

StableGS: A Floater-Free Framework for 3D Gaussian Splatting

Luchao Wang Qian Ren Kaiming He
Hua Wang Zhi Chen Yaohua Tang*

Moore Threads AI

Abstract

Recent years have witnessed remarkable success of 3D Gaussian Splatting (3DGS) in novel view synthesis, surpassing prior differentiable rendering methods in both quality and efficiency. However, its training process suffers from coupled opacity-color optimization that frequently converges to local minima, producing floater artifacts that degrade visual fidelity. We present StableGS, a framework that eliminates floaters through cross-view depth consistency constraints while introducing a dual-opacity GS model to decouple geometry and material properties of translucent objects. To further enhance reconstruction quality in weakly-textured regions, we integrate DUS_t3R depth estimation, significantly improving geometric stability. Our method fundamentally addresses 3DGS training instabilities, outperforming existing state-of-the-art methods across open-source datasets.

1. Introduction

Novel View Synthesis (NVS), aiming to reconstruct 3D scenes from monocular image collections and generate photorealistic novel views, plays a critical role in computer graphics and computer vision. A significant advancement was achieved by NeRF [14], which employs MLPs to model radiance fields combined with volume rendering. Subsequent works improved rendering quality [1–3] and speed [4, 15, 18], yet implicit representation methods face inherent limitations: rendering speed constrained by ray marching and fixed-capacity networks struggling with multi-scale geometry. 3D Gaussian Splatting (3DGS) [9] emerged as a new paradigm, explicitly parameterizing scenes with Gaussian ellipsoids to enable diverse scene representation and real-time rendering. While recent advancements like Mip-Splatting [22], GOF [23], and others [13, 25] enhanced reconstruction quality, persistent floater artifacts caused by irremovable outliers through gradient optimization remain observable.

*tangyaohua28@gmail.com

We thoroughly analyzed the floater issue and discovered that floaters stem from inherent properties of 3DGS’s rendering equation. Specifically, the coupling between Gaussian opacity α and color c parameters leads to overoptimization of color parameters, driving the model into local minima where floaters persist. To address this, we propose StableGS featuring two key innovations: 1) A depth consistency loss establishing cross-view depth mutual supervision to suppress floater generation; 2) A dual-opacity GS structure decoupling geometry and appearance for translucent objects, eliminating negative impacts introduced by depth constraints. Furthermore, we integrate DUS_t3R [19] depth priors through an efficient multi-frame optimization strategy, enabling robust initialization of 3DGS from Multi View Stereo(MVS) dense reconstruction while maintaining memory efficiency. This significantly enhances reconstruction quality in weakly-textured regions.

Our key contributions include:

- The first study to systematically investigate gradient vanishing caused by parameter coupling in 3DGS optimization and reveal fundamental limitations of the 3DGS rendering equation.
- A depth consistency loss for floater suppression and dual-opacity architecture to preserve translucent object quality.
- An efficient DUS_t3R-based dense reconstruction method for 3DGS initialization, enhanced by depth prior constraints for weak texture regions.
- The first work that completely eliminates floaters and achieves “the best” reconstruction results in the weakly-textured areas. Experimental results indicate that StableGS surpasses all the state-of-the-art approaches.

2. Relate Work

2.1. Novel View Synthesis

Novel View Synthesis (NVS) aims to infer unseen perspectives from monocular image collections. NeRF [14] pioneered MLP-based radiance field modeling with volume rendering, inspired extensive follow-up research. Subsequent works like NeRF++ [26], Mip-NeRF [1], and

Mip-NeRF360 [2] enhanced rendering quality, where Mip-NeRF360 achieved anti-aliasing through ray-cone encoding and suppressed floaters via distortion loss. Meanwhile, DVGO [18], Instant-NGP [15], and TensorRF [4] accelerated rendering to near real-time speeds. The emergence of 3DGS [9] established a new paradigm, employing explicit 3D Gaussian primitives to match Mip-NeRF360’s quality while significantly surpassing its efficiency, making it the current mainstream approach.

2.2. 3DGS Enhancements

3DGS [9] revolutionized NVS through rasterized Gaussian rendering with exceptional performance. Mip-Splatting [22] reduced aliasing artifacts via low-pass filtering, while densification strategy improvements emerged through absGS [20] (gradient absolute sum) and GOF [23] (combined gradient metrics). Geometric regularization approaches include 2DGS [8] projecting Gaussians to 2D surfaces and RadeGS [25] employing normal map constraints. Though some works [8, 25] adopt NeRF-style distortion loss for floater reduction, we demonstrate this approach inadequately addresses 3DGS-specific floaters by erroneously increasing outlier opacity. Learnable Signed Distance Field (SDF) based methods like GSDF [21] and SuGaR [6] mitigated floaters but suffered from resolution-dependent parameterization limiting scalability. The floater issue introduces color block artifacts into rendered images, degrading visual quality. However, no prior work has systematically investigated the root causes of this phenomenon, nor proposed effective solutions.

2.3. Dense Stereo Models

DUST3R [19] advanced depth estimation through pairwise pointmap prediction, leveraging inter-frame correspondence. Follow-up works include MAST3R [11] integrating keypoint matching and Splat3R [17] directly predicting 3DGS parameters. Our experiments identify DUST3R’s superior depth estimation accuracy, motivating its integration as depth prior guidance for 3DGS training.

3. Methodology

3.1. Preliminaries

Standard 3DGS represents scenes using learnable 3D Gaussian ellipsoids $\mathcal{G} = \{G_k\}_{k=1}^K$, where each Gaussian G_k is parameterized by $\{\alpha_k, \mu_k, q_k, s_k, c_k\}$. Here, $\alpha_k \in [0, 1]$ denotes opacity at the Gaussian center, $\mu_k \in \mathbb{R}^3$ specifies the center position, $q_k \in \mathbb{R}^4$ is a quaternion representing the rotation matrix $R_k \in \mathbb{R}^{3 \times 3}$, $s_k \in \mathbb{R}^3$ defines scaling factors through the diagonal matrix $S_k = \text{diag}(s_k) \in \mathbb{R}^{3 \times 3}$, $c_k \in \mathbb{R}^3$ corresponds to the color parameter. While standard 3DGS computes c_k via Spherical Harmonics, we directly employ c_k for color parameterization to simplify the prob-

lem. The opacity of Gaussian G_k at spatial point $x \in \mathbb{R}^3$ is given by:

$$\sigma_k(x) = \alpha_k \exp\left(-\frac{1}{2}(x - \mu_k)^\top \Sigma_k^{-1}(x - \mu_k)\right) \quad (1)$$

where $\Sigma_k = R_k S_k S_k^\top R_k^\top \in \mathbb{R}^{3 \times 3}$ is the covariance matrix controlling the ellipsoid’s spatial distribution.

For a ray $r(t) = \mathbf{o} + t\mathbf{d}$ ($t \geq 0$) [14], 3DGS employs a rasterization-based approach to render its color. The depth approximation of Gaussian G_k along the ray is given by projecting its center $d_k^r = \mathbf{d} \cdot (\mu_k - \mathbf{o})$, with the corresponding projected point $x_k^r = \mathbf{o} + d_k^r \mathbf{d}$. Assuming there are K_r Gaussians intersecting the ray, which are ordered by ascending d_k^r , the rendering equations become:

$$\bar{c}(r) = \sum_{k=1}^{K_r} c_k \sigma(x_k^r) \tau_k, \quad \bar{d}(r) = \sum_{k=1}^{K_r} d_k^r \sigma(x_k^r) \tau_k \quad (2)$$

where $\tau_k = \prod_{j=1}^{k-1} (1 - \sigma(x_j^r))$ and \bar{c} and \bar{d} denote the rendered color and depth values of the 3D Gaussian scene \mathcal{G} along ray r . Throughout this paper, $(\bar{\cdot})$ consistently indicates post-rendering results.

For an image frame I , let $O = \{r\}_{r \in I}$ denote its ray set. With ground truth pixel values C^{gt} , RGB image \bar{C} and depth map \bar{D} rendered by the 3DGS model \mathcal{G} , the base 3DGS loss combines:

$$\mathcal{L}_{\text{3DGS}} = (1 - \lambda) \mathcal{L}_1(\bar{C}, C^{\text{gt}}) + \lambda L_{\text{D-SSIM}}(\bar{C}, C^{\text{gt}}) \quad (3)$$

where $\mathcal{L}_1(\cdot)$ is the L1 loss and $L_{\text{D-SSIM}}(\cdot)$ denotes the SSIM loss.

3.2. StableGS

3.2.1. Floater Analysis in Gaussian Splatting

While 3DGS achieves efficient differentiable scene representation for novel view synthesis, its original implementation suffers from two critical flaws: **blurry problem** and **floater problem**. As shown in Fig. 1-(a), the first limitation manifests as blurry reconstructions of high-frequency details (e.g., grass textures), termed the blurry problem, stemming from insufficient Gaussian distributions due to failed densification strategies. The second limitation involves sporadic color artifact chunks (floater problem), caused by floating translucent Gaussians in free space. Adopting GOF’s densification strategy [23] mitigates blurry problem but exacerbates floaters. Fig. 1-(b) shows floaters emerging when applying GOF to originally clean Mip-Splatting [22]. Lowering densification thresholds also increases floaters, as seen in Fig. 1-(c) with halved thresholds in original 3DGS [9].

Our analysis identifies gradient vanishing during back-propagation as the fundamental cause of persistent floaters in fully trained models. To elucidate this mechanism, we construct a simplified scenario to explain why floaters cannot be eliminated through training. Consider a floater cluster comprising K_f Gaussians intersected by M rays $\{r_m\}_{m=1}^M$ with ground-truth colors $\{c_m^{\text{gt}}\}_{m=1}^M$. For simplicity, we assume

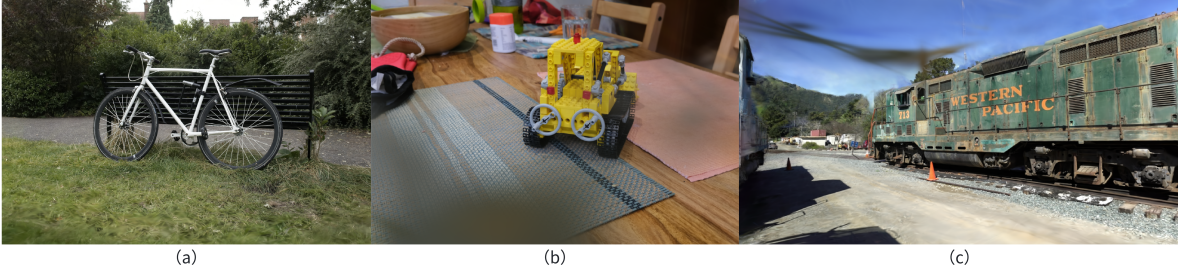


Figure 1. 3DGS suffers from blurry problem and floater problem. Fig. (a) shows the original 3DGS result, where model blurring occurs on the grassland. Fig. (b) presents the outcome of Mip-Splatting using GOF’s densification strategy, where it can be observed that while blurring is eliminated, floater artifacts are introduced. Fig. (c) demonstrates a modified version of the original 3DGS, with noticeable artifacts also appearing in the sky region of the image.

each ray traverses all K_f Gaussians and that non-floater regions of the scene have been fully optimized to match the ground truth. The rendered color for ray r_m is:

$$\bar{c}(r_m) = \sum_{k=1}^{K_f} c_k \sigma(x_k^{r_m}) \tau_k + c_m^{gt} \tau_{K_f+1} \quad (4)$$

Our optimization focuses solely on Gaussian opacity (α) and color (c) parameters to minimize the total color error $\sum_{m=1}^M \|\bar{c}(r_m) - c_m^{gt}\|$. Theoretically, the global optimum corresponds to $\{\alpha_k = 0\}_{k=1}^{K_f}$ with zero loss, yet empirical observations reveal frequent failures to converge to this solution — particularly with large K_f or high initial α_k values. Analysis of local minima demonstrates that floaters’ colors alpha blending result $c_f = \sum_{k=1}^{K_f} c_k \sigma(x_k^{r_m}) \tau_k$ satisfy $\sum_{m=1}^M \text{sign}(c_f - c_m^{gt}) \approx 0$ resulting in vanishing gradients for both $\{\alpha_k\}$ and $\{c_k\}$ through chain rule propagation. This phenomenon persists across L1, MSE, and cross-entropy loss functions. When K_f is large, the increased number of model parameters raises the risk of overfitting. The parameters $\{\alpha_k\}_{k=1}^{K_f}$, activated via sigmoid functions, exhibit slower optimization under high initial values due to sigmoid saturation. These factors collectively amplify the probability of converging to local minima.

This simplified experiment exposes an intrinsic limitation in 3DGS’s differentiable rendering formulation: over-optimization of color parameters induces local minima that degrade geometry optimization via opacity parameters, perpetuating unresolved floaters. Both GOF densification strategy refinements and lower densification thresholds exacerbate floater proliferation by spawning excessive Gaussians. Inspired by SDF-based methods, where SDF construction can be viewed as multi-view ray depth aggregation and SDF regularization enforces multi-view depth consistency, we validate through experiments that while $\{\alpha_k\}_{k=1}^{K_f}$ cannot guarantee convergence to zero, introducing depth loss functions effectively repels floater Gaussians, significantly diminishing their impact on final rendering.

3.2.2. Depth Consistency Loss

Building on the preceding analysis, we establish depth constraints as a principled solution to floater artifacts. This foundation motivates our Depth Consistency Loss design, which experimental results validate as effectively eliminating floaters. Unlike existing approaches like DNGaussian [12] that rely on monocular depth estimation — prone to scale ambiguity and geometric inaccuracy — we introduce dual-view depth mutual constraints. For frame pairs (i, j) (i and j are frame indexes), let \bar{D}_i, \bar{D}_j denote depth maps rendered by 3DGS model \mathcal{G} . The loss is defined as:

$$\mathcal{L}_{\text{consis}} = \sum_{(u,v) \in \mathcal{V}} (\|\mathcal{W}_{i \rightarrow j}(\bar{D}_i^{(u,v)}) - \bar{D}_j^{(u,v)}\|_1 + \|\mathcal{W}_{j \rightarrow i}(\bar{D}_j^{(u,v)}) - \bar{D}_i^{(u,v)}\|_1) \quad (5)$$

Here, \mathcal{V} denotes the valid projection region, and $\mathcal{W}_{i \rightarrow j}$ represents pose-based depth warping. This loss constrains consistency between depth maps rendered from paired frames. Floaters, represented as translucent Gaussian spheres in 3D space, render depth as the average of their own depth and background depth. Consequently, warped depth values will be projected to positions in other frames unaffected by floaters, thereby enabling correct supervision on floaters. This strategy assumes the scene contains no translucent objects — a premise inconsistent with real-world scenarios. Our approach for handling translucent objects is detailed in the following section.

Figure 2 demonstrates depth rendering results and warped comparisons from RadeGS training data. Row 1 shows rendered depth maps \bar{D}_i (with floater artifacts in the upper-left) and \bar{D}_j . Row 2 presents warped counterparts $\mathcal{W}_{j \rightarrow i}(\bar{D}_j)$ and $\mathcal{W}_{i \rightarrow j}(\bar{D}_i)$. In the second column, the coordinates corresponding to the floater in $\mathcal{W}_{i \rightarrow j}(\bar{D}_i)$ exhibit correct depth values in \bar{D}_j , providing an accurate reflection of the true geometric structure. Application of $\mathcal{L}_{\text{consis}}$ from Eq. (5) successfully rectifies these artifacts through cross-view depth consensus.

We select frame pairs from the training set using three criteria computed from the results of COLMAP, forming the pair set \mathcal{P} for the computation of $\mathcal{L}_{\text{consis}}$:

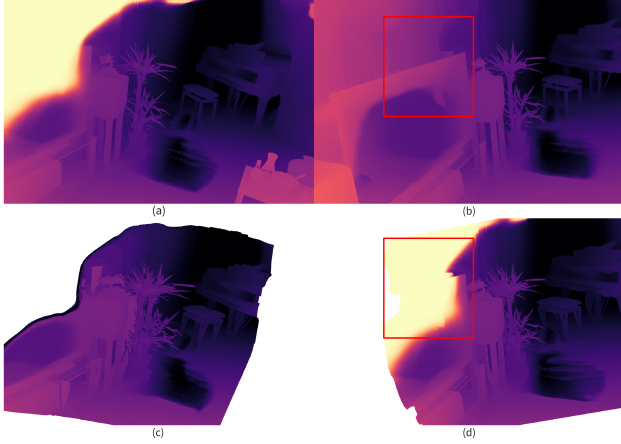


Figure 2. The figures show RadeGS rendering results of two example images from the room dataset training set (Fig. (a) and Fig. (b)) and their warped outcomes (Fig. (d) and Fig. (c)). A floater visible in the upper-left corner of Fig. (a) is projected into the red-boxed region of Fig. (d), while the corresponding red-boxed region in Fig. (b) displays accurate depth measurements. By enforcing constraints from Fig. (b) onto Fig. (d), the floater can be effectively eliminated.

- **Covisibility Constraint:** > 30 feature matches ensuring sufficient scene overlap
- **Angular Constraint:** Relative rotation angles between 16° and 60° to prevent insufficient/excessive viewpoint overlap
- **Motion Constraint:** Translation component ratio < 0.95 suppressing degeneracy from near-pure axial motion

3.2.3. Dual Opacity GS

Direct application of Depth Consistency Loss to vanilla 3DGS fails to handle translucent objects. To address this, we propose a dual-opacity Gaussian model augmented with auxiliary opacity parameters $\alpha'_k \in [0, 1]$. The revised spatial opacity function becomes:

$$\sigma'_k(x) = \alpha_k \alpha'_k \exp\left(-\frac{1}{2}(x - \mu_k)^\top \Sigma_k^{-1} (x - \mu_k)\right) \quad (6)$$

replacing the original formulation in Eq. (1). The model operates in two rendering modes. **Standard Mode** renders \bar{C}^s and \bar{D}^s using $\sigma(x)$ and **Dual-Opacity Mode** generates \bar{C}^o and \bar{D}^o via $\sigma'(x)$.

The base loss evolves from Eq. (3) to:

$$\mathcal{L}_{\text{color}} = \sum_{k \in \{i, j\}} (\mathcal{L}_{3\text{DGS}}(\bar{C}_k^o, C_k^{\text{gt}}) + \mathcal{L}_1(\bar{C}_k^s, C_k^{\text{gt}})) \quad (7)$$

The composite training objective combines:

$$\mathcal{L}_{\text{total}} = \mathcal{L}_{\text{color}} + \lambda_{\text{consis}} \mathcal{L}_{\text{consis}} \quad (8)$$

We introduce an L1 loss between \bar{C}^s and C^{gt} to focus auxiliary parameters α' on translucent materials unresolved by standard rendering. The depth consistency loss $\mathcal{L}_{\text{consis}}$ operates on \bar{D}^s outputs, leveraging the inequality $\sigma'(x) \leq \sigma(x)$ which ensures $\bar{D}^o \geq \bar{D}^s$. Since floaters exhibit abnormally shallow depths, enforcing the depth consistency loss on \bar{D}^s

inherently ensures the dual-opacity mode remains floater-free.

We name this enhanced model **StableGS**, which maintains the floater elimination capability of the depth consistency loss while incorporating the auxiliary parameter α'_k to render translucent materials, thereby ensuring the rendering quality of translucent objects.

3.3. Geometric Priors for Gaussian splatting

While the depth consistency loss $\mathcal{L}_{\text{consis}}$ effectively eliminates floater artifacts and enhances training stability, geometric recovery remains challenging in weakly-textured regions (e.g., white walls, uniformly lit surfaces). To address this, we integrate DUST3R depth estimation to improve reconstruction fidelity in such areas. We introduce an enhanced global optimization strategy for DUST3R, enabling efficient large-scale scene processing. This produces globally consistent depth priors to constrain the GS-rendered depth \bar{D} , while TSDF fusion [24] generates dense reconstructions for initializing 3DGS Gaussians.

3.3.1. DUST3R Depth Estimation

As described in the DUST3R paper [19], DUST3R processes two RGB frames I^1, I^2 to outputs two corresponding pointmaps $X^{1,1}, X^{2,1}$ with associated confidence maps $C^{1,1}, C^{2,1}$. both pointmaps are expressed in the same coordinate frame of I^1 . For compatibility with DUST3R’s 512-pixel long-edge constraint, we apply distortion removal and resizing via operator $\mathcal{R}(I)$. For any frame pair (i, j) , DUST3R outputs:

$$\Phi(i, j) \triangleq (X_{i,j}^{1,1}, X_{i,j}^{2,1}, C_{i,j}^{1,1}, C_{i,j}^{2,1}) \quad (9)$$

The complete output set across all frame pairs in \mathcal{P} is denoted as $\mathbb{X}^{\mathcal{P}} = \bigcup_{(i,j) \in \mathcal{P}} \{\Phi(i, j), \Phi(j, i)\}$.

3.3.2. Prior-Guided Depth Supervision

DUST3R’s per-pair processing yields inconsistent depth scales across pairs. Let $s_{i,j}$ denote the scale factor for $\Phi(i, j)$. We optimize all scales $S = \{(s_{i,j}, s_{j,i})\}_{(i,j) \in \mathcal{P}}$ for $\mathbb{X}^{\mathcal{P}}$ to achieve global consistency. Given COLMAP-estimated camera poses $\{T^i\}_{i=1}^N$ and world-coordinate pointmaps $\{X^{i,W}\}_{i=1}^N$ (N : total frames), we formulate the optimization from base DUST3R as:

$$\min_{\{X^{i,W}\}_{i=0}^N, S} \sum_{(i,j) \in \mathcal{P}} [\mathcal{E}(i, j) + \mathcal{E}(j, i)], \quad (10)$$

$$\text{where } \mathcal{E}(i, j) = \left\| \left[\begin{array}{c} C_{i,j}^{1,1} \odot (X^{i,W} - s_{i,j} T^i X_{i,j}^{1,1}) \\ C_{i,j}^{2,1} \odot (X^{j,W} - s_{i,j} T^i X_{i,j}^{2,1}) \end{array} \right] \right\|$$

where \odot denotes element-wise multiplication. Homogeneous coordinates are assumed for X terms, with the fourth dimension ignored in loss computation. Through variable substitution to eliminate $\{X^{i,W}\}_{i=0}^N$, we obtain the equivalent optimization problem:

$$\min_S \sum_{(i,j) \in \mathcal{P}} \|\mathcal{C}(i,j), \mathcal{C}(j,i)\| \odot ([s_{i,j}T^i, -s_{j,i}T^j]\mathcal{X})\|$$

$$\text{where } \mathcal{C}(i,j) = \frac{C_{i,j}^{1,1}C_{j,i}^{2,1}}{C_{i,j}^{1,1} + C_{j,i}^{2,1}}, \mathcal{X} = \begin{bmatrix} X_{i,j}^{1,1} & X_{i,j}^{2,1} \\ X_{j,i}^{2,1} & X_{j,i}^{1,1} \end{bmatrix}$$

The original formulation requires maintaining $\mathbb{X}^{\mathcal{P}}$ in GPU memory, which remains computationally prohibitive. We propose a matrix factorization-based equivalent point reduction strategy, decomposing pairwise pointmaps matching problem into compact 7-point representations: $x_{i,j} \in \mathbb{R}^{7 \times 3}$ and $y_{i,j} \in \mathbb{R}^{7 \times 3}$ are the equivalent points for view i and j , $w_{i,j} \in \mathbb{R}^{1 \times 7}$ is the corresponding confidence weights. The global optimization problem thus reduces to:

$$\min_S \sum_{(i,j) \in \mathcal{P}} \|w_{i,j} \odot ([s_{i,j}T^i - s_{j,i}T^j][x_{i,j}, y_{i,j}]^T)\| \quad (11)$$

Equivalence Proof: For a general weighted point set matching problem formulated as $\|\mathcal{J} \odot (A_1Y_1^T + b_1 - A_2Y_2^T - b_2)\|$, where $A_1, A_2 \in \mathbb{R}^{3 \times 3}$ and $b_1, b_2 \in \mathbb{R}^{3 \times 1}$ represent arbitrary 3D affine transformations, $Y_1, Y_2 \in \mathbb{R}^{N \times 3}$ denote source and target points, and $\mathcal{J} \in \mathbb{R}^{1 \times N}$ denotes weights. Let $b = b_1 - b_2$, the formulation can be equivalently expressed as:

$$\begin{aligned} & \|\mathcal{J} \odot ([A_1, -A_2, b][Y_1, Y_2, 1]^T)\| \\ &= [A_1, -A_2, b][Y_1, Y_2, 1]^T \text{diag}(\mathcal{J}^2)[Y_1, Y_2, 1][A_1, -A_2, b]^T \\ &= [A_1, -A_2, b]V^T \text{diag}(\xi^2)V[A_1, -A_2, b]^T \end{aligned}$$

where $V^T \text{diag}(\xi^2)V$ constitutes the eigenvalue decomposition of the bracketed term, with $V \in \mathbb{R}^{7 \times 7}$ and $\xi \in \mathbb{R}^7$. This can be reformulated into a point-matching form $\|w \odot ([A_1, -A_2, b][x, y, 1]^T)\|$, where $w = \xi V_{[:,7]}$, $x = V_{[:,1-3]}/V_{[:,7]}$, and $y = V_{[:,4-6]}/V_{[:,7]}$, with $V_{[:,i]}$ denoting corresponding columns of V .

Optimizing via Eq. (11) yields scale factors S , from which we derive $\mathcal{D}_{\text{DUS3R}} = \{(d_{i,j}, d_{j,i}, w_{i,j}, w_{j,i})\}_{(i,j) \in \mathcal{P}}$, where $d_{i,j} = s_{i,j}X_{i,j[2]}^{1,1}$ and $w_{i,j} = C_{i,j}^{1,1}$. Since $X_{i,j[2]}^{1,1}$ represents the z -coordinate of the point cloud and $X_{i,j}^{1,1}$ resides in the camera coordinate system, it is equivalent to the depth map. The terms $d_{j,i}$ and $w_{j,i}$ are derived analogously.

While Eq. (11) theoretically supports camera pose optimization $\{T^i\}_{i=1}^N$, DUS3R’s inherent depth errors limit practical pose refinement. Nevertheless, our method achieves superior stability in global Structure-from-Motion (SFM) [5] without initial poses, outperforming GLOMAP [16] in reconstruction success rates. Future work will unify global SFM and MVS using DUS3R-derived constraints.

Following offline computation of $\mathcal{D}_{\text{DUS3R}}$, we define a depth prior loss to constrain 3DGS-rendered results. For

frame pairs $(i, j) \in \mathcal{P}$, the loss is formulated as:

$$\begin{aligned} \mathcal{L}_{\text{prior}} &= \frac{1}{\|d_{i,j}\|_0} \sum_{\text{pixel}} w_{i,j} \odot |\mathcal{R}(\bar{D}_i^s) - d_{i,j}| \\ &+ \frac{1}{\|d_{j,i}\|_0} \sum_{\text{pixel}} w_{j,i} \odot |\mathcal{R}(\bar{D}_j^s) - d_{j,i}| \end{aligned} \quad (12)$$

The composite loss function is now defined as:

$$\mathcal{L}_{\text{total}} = \mathcal{L}_{\text{color}} + \lambda_{\text{consis}}\mathcal{L}_{\text{consis}} + \lambda_{\text{prior}}\mathcal{L}_{\text{prior}} \quad (13)$$

Here, $\|\cdot\|_0$ denotes the zero-norm (count of non-zero elements) and $|\cdot|$ represents absolute value computation. Optimizing $\mathcal{L}_{\text{prior}}$ enables the model to learn geometric structures in weakly-textured regions while benefiting from enhanced robustness through depth priors.

Similar to the depth consistency loss, we constrain \bar{D}^s instead of \bar{D}^o . The inaccuracies in depth estimation result in precision loss in \bar{D}^s , while the details are recovered in \bar{D}^o . This phenomenon will be demonstrated in our ablation experiments.

3.3.3. Dense Reconstruction for Initialization

Given 3DGS’s sensitivity to initialization, we integrate MVS via DUS3R to construct dense reconstructions for 3DGS initialization, enhancing geometric recovery — particularly in weakly-textured regions. Our pipeline first refines DUS3R depth maps, and utilizes TSDF Fusion [24] to conduct dense 3D reconstruction.

We propose a learnable depth correction function $\phi(d; r, l) = d^r + l \cdot d$ to mitigate noise in DUS3R-predicted depth maps. Leveraging COLMAP’s sparse 3D keypoints, we project them into corresponding camera coordinate systems. For frame i , the projected 3D points on the image plane are represented as $\mathcal{K}_i = \{(u_i^k, v_i^k, d_i^k)\}$, where (u_i^k, v_i^k) denotes the image coordinates of the k -th keypoint, and d_i^k its depth value in frame i ’s camera frame. We formulate:

$$\min_{S, \Theta_\phi} \sum_{(i,j) \in \mathcal{P}} \left(\sum_{k \in \mathcal{K}_i} c_{i,j}^k |s_{i,j}\phi(d_{i,j}^k; r_{i,j}, l_{i,j}) - d_i^k| + \sum_{k \in \mathcal{K}_j} c_{j,i}^k |s_{j,i}\phi(d_{j,i}^k; r_{j,i}, l_{j,i}) - d_j^k| \right)$$

$$\text{where } \begin{cases} c_{i,j}^k = C_{i,j}^{1,1}(u_i^k, v_i^k) \\ d_{i,j}^k = X_{i,j[2]}^{1,1}(u_i^k, v_i^k) \\ \Theta_\phi = \{r_{i,j}, r_{j,i}, l_{i,j}, l_{j,i}\}_{(i,j) \in \mathcal{P}} \end{cases}$$

After optimization, refined depth maps are obtained. For frame pairs (i, j) : $d_{i,j}^{\text{refine}} = s_{i,j}\phi(X_{i,j[2]}^{1,1}, r_{i,j}, l_{i,j})$, and $d_{j,i}^{\text{refine}}$ is derived similarly. For all pairs \mathcal{P} , the weighted depth maps form the set: $\mathcal{D}_{\text{refine}} = \{(d_{i,j}^{\text{refine}}, d_{j,i}^{\text{refine}}, w_{i,j}, w_{j,i})\}_{(i,j) \in \mathcal{P}}$. Using $\mathcal{D}_{\text{refine}}$, we perform weighted TSDF fusion to reconstruct the scene and generate the corresponding mesh.

Notably, depth map estimations perform poorly for distant backgrounds. During 3DGS initialization, we include

Table 1. Performance comparison on mipnerf360, Blender and Tanks&Temples.

Architecture	mipnerf360 indoor			mipnerf360 outdoor			Blender			Tanks&Temples		
	PSNR↑	SSIM↑	LPIPS↓	PSNR↑	SSIM↑	LPIPS↓	PSNR↑	SSIM↑	LPIPS↓	PSNR↑	SSIM↑	LPIPS↓
3DGS [9]	30.458	0.9170	0.1975	26.644	0.8063	0.1835	29.732	0.9054	0.2422	23.562	0.8465	0.18020
Mip-Splatting [22]	30.971	0.9242	0.1870	26.384	0.7912	0.2051	29.622	0.9050	0.2431	23.836	0.8531	0.17370
Taming-3DGS [13]	31.107	0.9225	0.1926	26.645	0.7997	0.1948	29.599	0.9065	0.2395	24.017	0.8546	0.17320
GOF [23]	30.465	0.9178	0.1888	26.566	0.8052	0.1852	29.569	0.9059	0.2427	23.592	0.8530	0.16820
RadeGS [25]	30.509	0.9213	0.1887	26.709	0.8119	0.1753	29.530	0.9073	0.2416	23.897	0.8560	0.16725
StableGS	31.112	0.9222	0.1892	26.705	0.8110	0.1784	29.545	0.9071	0.2378	23.861	0.8548	0.16425
+ $\mathcal{L}_{\text{prior}}$	31.191	0.9245	0.1838	26.702	0.8120	0.1709	29.688	0.9073	0.2385	23.969	0.8550	0.16325
+ $\mathcal{L}_{\text{prior}}$ +DenseInit	31.122	0.9246	0.1829	26.713	0.8133	0.1678	29.658	0.9065	0.2375	24.039	0.8560	0.16180

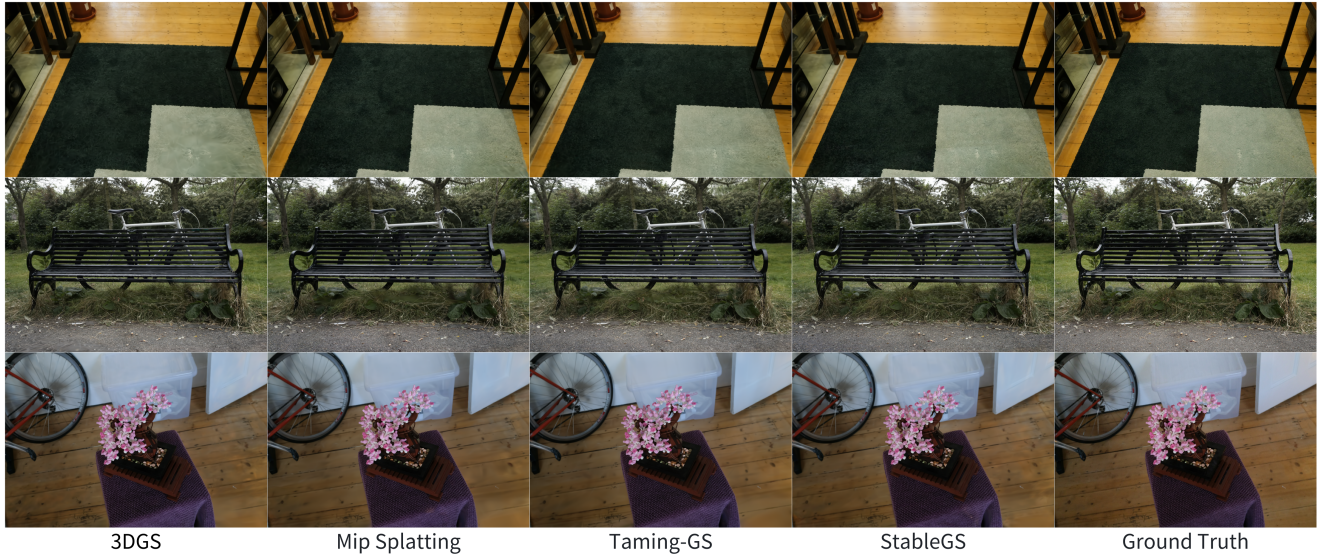


Figure 3. **blurry problem.** Our method outperforms previous methods in addressing the blurring problem. Note the first row texture details of the carpet, the second row grass beneath the chair, and the third row floor details (particularly in the lower-right corner region)

keypoints outside the TSDF boundary into the initialization points.

4. Experiments

4.1. Experimental setting

This work implements differentiable depth rendering based on RadeGS [25]. All experiments train for 30,000 iterations with unified settings. Gaussian densification strategy is from GOF [23], gradient threshold is 0.002 and learning rates and other hyperparameters match original 3DGS. We have three comparative settings:

- **StableGS:** Dual-opacity GS architecture with $\mathcal{L}_{\text{consis}}$ ($\lambda_{\text{consis}} = 0.05$)
- **StableGS+ $\mathcal{L}_{\text{prior}}$:** Adds depth prior loss $\mathcal{L}_{\text{prior}}$ ($\lambda_{\text{prior}} = 0.005$)
- **StableGS+ $\mathcal{L}_{\text{prior}}$ +DenseInit:** Further initializes with MVS-reconstructed dense point clouds

4.2. Datasets

This experiment validates method effectiveness on three standard datasets:

- **Mip-NeRF360 [2]:** Contains 4 indoor and 3 outdoor scenes. We train at half resolution with the longest edge

limited to 1600 pixels (larger images are aspect-ratio scaled).

- **Deep Blending [7]:** Two complex lighting scenes (Dr.Johnson and Playroom) are selected.
- **Tanks&Temples [10]:** Train and Truck scenes evaluate large-scale scene reconstruction capability.

4.3. Comparison

Consistent with prior work [9], we adopt PSNR, SSIM, and LPIPS [27] as image quality metrics. Our comparisons include: original 3DGS [9], Mip-Splatting [22], Taming-3DGS [13], GOF [23], and RadeGS [25]. For Taming-3DGS, point counts match our StableGS results. The results in Tab. 1 demonstrate our method’s consistent superiority over existing approaches.

We demonstrate our method’s superiority through three aspects: blurry problem, floater problem, and weakly-textured region reconstruction. Case studies confirm that prior methods exhibit either blurry or floater issues, while our StableGS eliminates blur without introducing floaters. Furthermore, by incorporating geometric priors, our approach achieves state-of-the-art results in weakly-textured regions.

Blurry Problem: We compare 3DGS, Mip-Splatting, Taming-3DGS, and our StableGS. Figure 3 shows that orig-

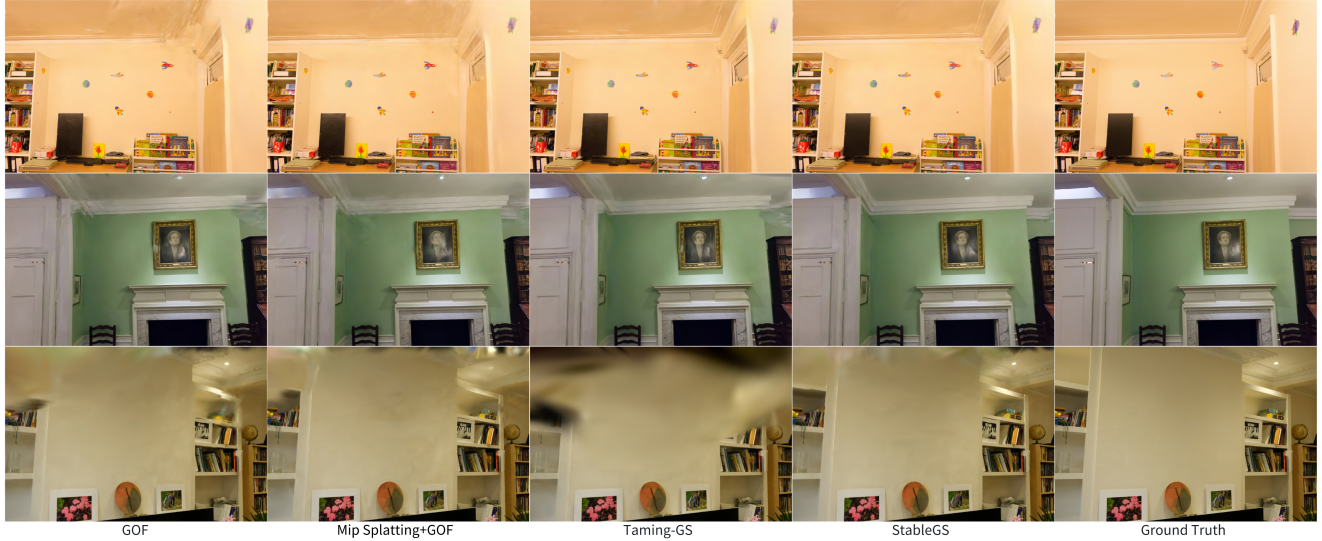


Figure 4. **floater problem.** Our method outperforms previous methods in addressing the floater problem. Note the first row ceiling and upper-right wall region, the second row prominent artifacts in the upper-left and upper-right corners; and the third row wall surfaces.

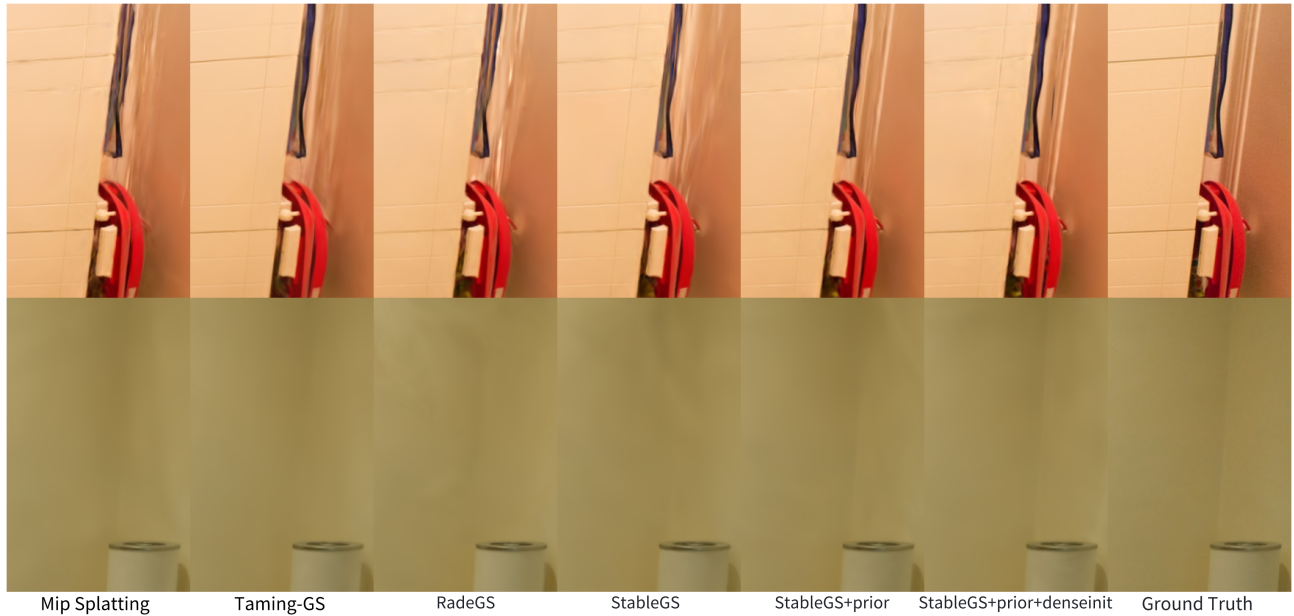


Figure 5. **Weakly-Textured Region Reconstruction.** Our method outperforms previous approaches in reconstructing weakly-textured regions. Note the first row clarity of vertical textures and the second row vertical lines at wall junction regions.

inal 3DGS exhibits significant blur, Mip-Splatting exacerbates blur despite resolving aliasing, Taming-3DGS retains blur despite densification improvements, but StableGS delivers the sharpest results.

Floater Problem: We compare GOF, Mip-Splatting+GOF (Mip-Splatting with GOF densification strategy), RadeGS, and our StableGS. In this comparative group, all methods adopt the GOF densification strategy. Figure 4 show that while other methods exhibit varying degrees of floaters, our approach remains notably floater-free.

Weakly-Textured Region Reconstruction: By introducing depth prior loss and dense reconstruction ini-

tialization, we enhance reconstruction quality in weakly-textured regions. This experiment compares rendering performance of Mip-Splatting [22], Taming-3DGS [13], and RadeGS [25] in such regions. To demonstrate the efficacy of our depth prior loss and dense initialization, we further present comparative results across three configurations: StableGS, StableGS+ $\mathcal{L}_{\text{prior}}$, and StableGS+ $\mathcal{L}_{\text{prior}}$ +DenseInit. Figure 5 show StableGS+ $\mathcal{L}_{\text{prior}}$ +DenseInit achieves the best performance, producing the sharpest edges in challenging areas like wall corners.



Figure 6. **Dense Reconstruction Results.** Our dense reconstruction results are displayed. The first row presents the reconstructed texture, while the second row shows geometry-aware shading renderings. These results clearly demonstrate that our reconstruction faithfully reproduces both the scene’s color textures and geometric structures.

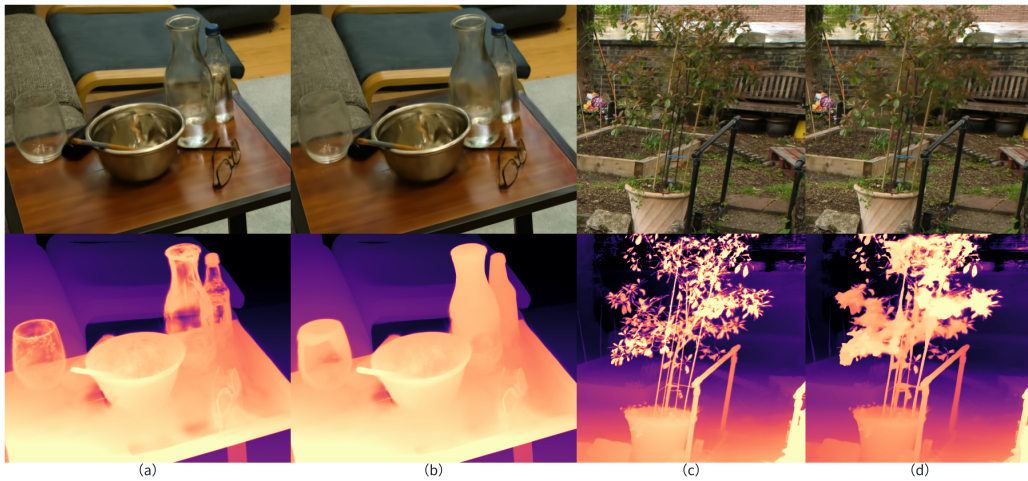


Figure 7. Figs. (a)-(b) illustrate the depth consistency loss effectively decouples geometry and material properties in translucent objects; Figs. (c)-(d) demonstrate the dual-opacity GS model’s capability to mitigate detail loss.

4.4. Dense Reconstruction Results

We demonstrate MVS dense reconstruction outcomes achieved through our optimization pipeline. All scenes are reconstructed using DUS3R-estimated depth maps refined by our global optimization and depth correction, followed by TSDF fusion. Benefiting from DUS3R’s inherent efficiency and our streamlined optimization, processing each scene requires only a few minutes. All results use a unified TSDF voxel size of 0.05. Figure 6 demonstrates our reconstructions faithfully recover scene textures and geometric structures, as visually verified.

4.5. Ablation studies

This section experimentally analyzes the impacts of the depth consistency loss and depth prior loss.

Depth Consistency Loss We demonstrate the depth consistency loss’s effect on translucent objects and our dual-opacity architecture’s ability to disentangle translucent materials. As shown in the Figure 7 (a)-(b): Figs. (a) displays dual-opacity mode renderings, while Figs. (b) shows stan-

dard mode results. In standard mode depth maps, glass bottles appear as opaque solids, confirming our method correctly learns translucent object geometry — albeit at the cost of reduced image quality, evidenced by blurred specular effects on bottle surfaces in RGB outputs. Dual-opacity mode restores transparency in depth maps while preserving other objects’ integrity, proving α' successfully captures translucent material opacity.

Depth Prior Loss. We demonstrate the precision degradation introduced by the depth prior loss and our dual-opacity architecture’s ability to counteract it. As shown in the Figure 7 (c)-(d): Figs. (d) shows standard mode renderings — depth maps exhibit detail loss, with corresponding blur in RGB images. In contrast, our dual-opacity mode (Figs. (c)) maintains accurate depth estimation and sharper RGB reconstructions.

5. Conclusion

Our analysis of 3D Gaussian Splatting (3DGS) training reveals inherent local minima issues caused by gradient van-

ishing in rasterization-based rendering optimization, preventing effective floater elimination. To address this issue, we propose an improved method, StableGS. This approach introduces dual-opacity GS and depth consistency loss, effectively resolving the floater problem. Building on this, we further integrate the DUST3R method, incorporating depth prior loss and initializing 3DGS with DUST3R’s complete dense reconstruction results. This enhancement significantly improves reconstruction quality in weakly-textured regions. Our method demonstrates superior performance compared to current SOTA approaches. In contrast to existing methods, our method solve both the blurry problem and floater problem, while achieving higher image quality in weakly-textured regions.

References

- [1] Jonathan T Barron, Ben Mildenhall, Matthew Tancik, Peter Hedman, Ricardo Martin-Brualla, and Pratul P Srinivasan. Mip-nerf: A multiscale representation for anti-aliasing neural radiance fields. In *Proceedings of the IEEE/CVF international conference on computer vision*, pages 5855–5864, 2021. 1
- [2] Jonathan T Barron, Ben Mildenhall, Dor Verbin, Pratul P Srinivasan, and Peter Hedman. Mip-nerf 360: Unbounded anti-aliased neural radiance fields. In *Proceedings of the IEEE/CVF conference on computer vision and pattern recognition*, pages 5470–5479, 2022. 2, 6
- [3] Jonathan T Barron, Ben Mildenhall, Dor Verbin, Pratul P Srinivasan, and Peter Hedman. Zip-nerf: Anti-aliased grid-based neural radiance fields. In *Proceedings of the IEEE/CVF International Conference on Computer Vision*, pages 19697–19705, 2023. 1
- [4] Anpei Chen, Zexiang Xu, Andreas Geiger, Jingyi Yu, and Hao Su. Tensorf: Tensorial radiance fields. In *European conference on computer vision*, pages 333–350. Springer, 2022. 1, 2
- [5] Zhaopeng Cui and Ping Tan. Global structure-from-motion by similarity averaging. In *Proceedings of the IEEE international conference on computer vision*, pages 864–872, 2015. 5
- [6] Antoine Guédon and Vincent Lepetit. Sugar: Surface-aligned gaussian splatting for efficient 3d mesh reconstruction and high-quality mesh rendering. In *Proceedings of the IEEE/CVF Conference on Computer Vision and Pattern Recognition*, pages 5354–5363, 2024. 2
- [7] Peter Hedman, Julien Philip, True Price, Jan-Michael Frahm, George Drettakis, and Gabriel Brostow. Deep blending for free-viewpoint image-based rendering. *ACM Transactions on Graphics (ToG)*, 37(6):1–15, 2018. 6
- [8] Binbin Huang, Zehao Yu, Anpei Chen, Andreas Geiger, and Shenghua Gao. 2d gaussian splatting for geometrically accurate radiance fields. In *ACM SIGGRAPH 2024 conference papers*, pages 1–11, 2024. 2
- [9] Bernhard Kerbl, Georgios Kopanas, Thomas Leimkühler, and George Drettakis. 3d gaussian splatting for real-time radiance field rendering. *ACM Trans. Graph.*, 42(4):139–1, 2023. 1, 2, 6
- [10] Arno Knapitsch, Jaesik Park, Qian-Yi Zhou, and Vladlen Koltun. Tanks and temples: Benchmarking large-scale scene reconstruction. *ACM Transactions on Graphics (ToG)*, 36(4): 1–13, 2017. 6
- [11] Vincent Leroy, Yohann Cabon, and Jérôme Revaud. Grounding image matching in 3d with mast3r. In *European Conference on Computer Vision*, pages 71–91. Springer, 2024. 2
- [12] Jiahe Li, Jiawei Zhang, Xiao Bai, Jin Zheng, Xin Ning, Jun Zhou, and Lin Gu. Dngaussian: Optimizing sparse-view 3d gaussian radiance fields with global-local depth normalization. In *Proceedings of the IEEE/CVF conference on computer vision and pattern recognition*, pages 20775–20785, 2024. 3
- [13] Saswat Subhajyoti Mallick, Rahul Goel, Bernhard Kerbl, Markus Steinberger, Francisco Vicente Carrasco, and Fernando De La Torre. Taming 3dgs: High-quality radiance fields with limited resources. In *SIGGRAPH Asia 2024 Conference Papers*, pages 1–11, 2024. 1, 6, 7
- [14] Ben Mildenhall, Pratul P Srinivasan, Matthew Tancik, Jonathan T Barron, Ravi Ramamoorthi, and Ren Ng. Nerf: Representing scenes as neural radiance fields for view synthesis. *Communications of the ACM*, 65(1):99–106, 2021. 1, 2
- [15] Thomas Müller, Alex Evans, Christoph Schied, and Alexander Keller. Instant neural graphics primitives with a multiresolution hash encoding. *ACM transactions on graphics (TOG)*, 41(4):1–15, 2022. 1, 2
- [16] Linfei Pan, Daniel Barath, Marc Pollefeys, and Johannes Lutz Schönberger. Global Structure-from-Motion Revisited. In *European Conference on Computer Vision (ECCV)*, 2024. 5
- [17] Brandon Smart, Chuanxia Zheng, Iro Laina, and Victor Adrian Prisacariu. Splatt3r: Zero-shot gaussian splatting from uncalibrated image pairs. *arXiv preprint arXiv:2408.13912*, 2024. 2
- [18] Cheng Sun, Min Sun, and Hwann-Tzong Chen. Direct voxel grid optimization: Super-fast convergence for radiance fields reconstruction. In *Proceedings of the IEEE/CVF conference on computer vision and pattern recognition*, pages 5459–5469, 2022. 1, 2
- [19] Shuzhe Wang, Vincent Leroy, Yohann Cabon, Boris Chidlovskii, and Jerome Revaud. Dust3r: Geometric 3d vision made easy. In *Proceedings of the IEEE/CVF Conference on Computer Vision and Pattern Recognition*, pages 20697–20709, 2024. 1, 2, 4
- [20] Zongxin Ye, Wenyu Li, Sidun Liu, Peng Qiao, and Yong Dou. Absgs: Recovering fine details in 3d gaussian splatting. In *Proceedings of the 32nd ACM International Conference on Multimedia*, pages 1053–1061, 2024. 2
- [21] Mulin Yu, Tao Lu, Linning Xu, Lihan Jiang, Yuanbo Xiangli, and Bo Dai. Gsdf: 3dgs meets sdf for improved rendering and reconstruction. *arXiv preprint arXiv:2403.16964*, 2024. 2
- [22] Zehao Yu, Anpei Chen, Binbin Huang, Torsten Sattler, and Andreas Geiger. Mip-splatting: Alias-free 3d gaussian splatting. In *Proceedings of the IEEE/CVF conference on computer vision and pattern recognition*, pages 19447–19456, 2024. 1, 2, 6, 7

- [23] Zehao Yu, Torsten Sattler, and Andreas Geiger. Gaussian opacity fields: Efficient adaptive surface reconstruction in unbounded scenes. *ACM Transactions on Graphics (TOG)*, 43(6):1–13, 2024. [1](#), [2](#), [6](#)
- [24] Andy Zeng, Shuran Song, Matthias Nießner, Matthew Fisher, Jianxiong Xiao, and Thomas Funkhouser. 3dmatch: Learning local geometric descriptors from rgb-d reconstructions. In *CVPR*, 2017. [4](#), [5](#)
- [25] Baowen Zhang, Chuan Fang, Rakesh Shrestha, Yixun Liang, Xiaoxiao Long, and Ping Tan. Rade-gs: Rasterizing depth in gaussian splatting. *arXiv preprint arXiv:2406.01467*, 2024. [1](#), [2](#), [6](#), [7](#)
- [26] Kai Zhang, Gernot Riegler, Noah Snavely, and Vladlen Koltun. Nerf++: Analyzing and improving neural radiance fields. *arXiv preprint arXiv:2010.07492*, 2020. [1](#)
- [27] Richard Zhang, Phillip Isola, Alexei A Efros, Eli Shechtman, and Oliver Wang. The unreasonable effectiveness of deep features as a perceptual metric. In *CVPR*, 2018. [6](#)